Journal of
Mechanical
Science and
Technology

Journal of Mechanical Science and Technology 21 (2007) 1901~1909

Flow characteristics along and above dimpled surfaces with three different dimple depths within a channel

S. Y. Won[1,*] and P. M. Ligrani[2]

[1]*Nuclear Engineering & Technology Institute, Korea Hydro & Nuclear Power Co. Ltd., Korea*
[2]*Department of Engineering Science, University of Oxford, England, United Kingdom*

(Manuscript Received May 7, 2007; Revised July 19, 2007; Accepted July 19, 2007)

Abstract

The effects of dimples in altering time-averaged flow behavior occur mostly within one-half of one dimple print diameter from the surface, and the dimples within the arrays periodically eject a primary vortex pair from each dimple, which exists in conjunction with edge vortex pairs that form along the spanwise edges of staggered dimples regardless of three dimple depths. As the dimple depth increases, deeper dimples eject stronger primary vortex pairs, with hig her levels of turbulence transport due to larger deficits of time-averaged, normalized total pressure and streamw ise velocity as the surfaces with deeper dimples are approached. Primary vortex pair ejection frequencies range about 7-9 Hz, and edge vortex pair oscillation frequencies range about 5-7 Hz for Re_H=20,000, regardless of dimple depths.

Keywords: Dimple depth; Flow visualization; Reynold normal stress; Primary vortex pair; Edge vortex pair

1. Introduction

Dimples are used on the surfaces of internal flow passages because they produce substantial heat transfer augmentations, with pressure drop penalties that are smaller than many other types of heat augmentation devices, such as pin fins and rib turbulators. Such dimpled passages are useful for a variety of practical applications, such as internal cooling passages of turbine blades and vanes employed in gas turbine engines, electronic cooling, heat exchangers, micro-scale passages, bio-medical devices, and combustion chamber liners. Arrays of dimples accomplish this: (i) by ejecting multiple pairs of vortices, which increases secondary advection, and local, three-dimensional turbulence transport, as they advect downstream, and (ii) by not protruding into the flow, and therefore, by not increasing losses due to form drag [1-3]. Also important are the unsteadiness associated with vortex pair shedding, and the reattachment of the shear layer that forms across the top of each dimple. Dimples are also attractive heat transfer augmentation devices because they generally require uncomplicated manufacturing procedures, particularly if the dimple shape is a spherical indentation.

Recent dimple investigations employ flows over flat walls with regular arrays of spherical pits [1], flows in annular passages with a staggered array of concave dimples on the interior cylindrical surface [2], flows in single hemispherical cavities [3, 4], flows in diffuser and convergent channels each with a single hemispherical cavity [5], and flows in a narrow channel with spherically shaped dimples placed in relative positions on two opposite surfaces [6]. A computational simulation of flows over dimpled surfaces in a channel gives flow structures, flow streamlines, temperature distributions, and resulting surface heat transfer distributions for similar geo-

*Corresponding author. Tel.: +82 42 870 5532, Fax.: +82 42 870 5539
E-mail address: w1310@khnp.co.kr

metries and flow conditions [7]. Moon et al. [8] give data that show that improvements in heat transfer intensification and pressure losses remain at approximately constant levels for different Reynolds numbers and channel heights. Mahmood et al. [9] describe the mechanisms responsible for local and spatially-averaged heat transfer augmentations on flat channel surfaces with an array of dimples on one wall for one channel height equal to 50 percent of the dimple print diameter. Other recent investigations consider flow and heat transfer in single spherical cavities [10], effects of dimples and protrusions on opposite channel walls [11, 12], the effects of dimple depth on vortex structure and surface heat transfer [13, 14], the effects of deep dimples on local surface Nusselt number distributions [15], the combined influences of aspect ratio, temperature ratio, Reynolds number, and flow structure [16], and the flow structure due to dimple depressions on a channel surface [17].

The present study provides the flow characteristics along and above dimpled surfaces with non dimensional dimple depths, δ/D, from 0.1 to 0.3 (where δ is dimple depth, D is dimple print diameter). The data investigated are obtained from instantaneous flow visualization images, time-averaged flow structural characteristics surveys of different quantities, Reynolds normal stress, power spectra density of longitudinal velocity fluctuations, and vortex information frequency information using a five-hole pressure probe and hot wire anemometry probe.

2. Experimental apparatus and procedures

2.1 Dimpled test surface

The overall experimental apparatus for flow visualizations and flow structural measurements along and above dimpled surfaces with different dimple depths (but not the test section) are similar to the one described by Mahmood et al. [9].

Fig. 1(a) shows geometric details of the test section, including the dimpled test surface at the bottom and the top smooth surface at the top. Dimple geometries are then given in Fig. 1(b) in detail. In the present study, a total of 29 rows of dimples are employed in the streamwise direction, with 4 or 5 dimples in each row. These dimples are positioned on the surface in a staggered array. Also, the coordinate system of the test section is identified in Fig. 1(a). Note that the Y coordinate is normal from the test surface.

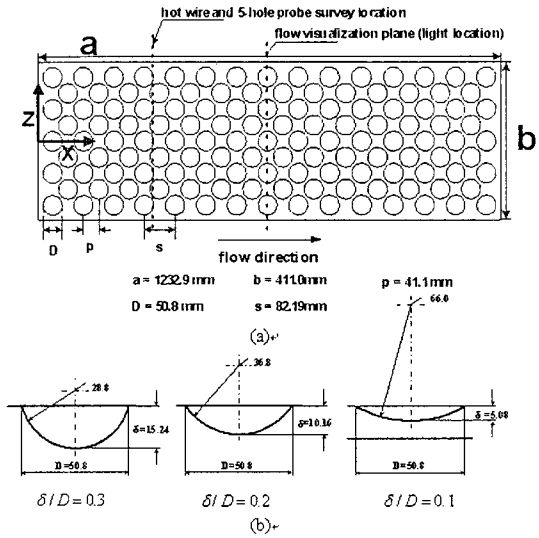

Fig. 1. Schematic diagrams of (a) the arrangement and placement of dimpled test surface, and (b) cross-sectional details of deep, medium and shallow dimples, respectively. All dimensions are given in mm.

2.2 Flow visualization of instantaneous flow structure

Flow visualization using smoke is used to identify vortex structures and other secondary flow features. Smoke from three horizontally-oriented smoke wires is employed for this purpose. These are located 6.0 mm, 12.0 mm, and 18.0 mm from the bottom test surface at X=205.5 mm, which is above the center of the fifth dimple row along the shallow dimple test surface. To produce sheets of smoke, each wire is first coated with Barts Pneumatics Corp. super smoke fluid and then powered by a Hewlett-Packard 6433B DC power supply. With this arrangement, the smoke forms into single thin planes parallel to the test surface. As the smoke is advected downstream, the secondary flows which accompany vortex and secondary flow development cause the smoke to be rearranged in patterns which show the locations and distributions of these flow phenomena. Smoke patterns are illuminated in spanwise-normal light planes located at X=616.5 mm (above the center of the fifteenth dimple row) with a thin sheet of light provided by a Colotran ellipsoidal No. 550, 1000 Watt spot light, and slits machined in two parallel metal plates. Images are recorded with a Panasonic WV-BP330 CCTV video camera. The analog images

from this camera are acquired and then digitized by using a Scion Image Corporation Frame grabber video card, and Scion image v.1.9.2 software. The resulting images are then further processed with a Dell P4 Precision 330 PC computer. Additional discussion of many of the procedures used for flow visualization is provided by Ligrani [18].

2.3 Time-averaged flow velocity components and pressure

A 1.27 mm diameter miniature five-hole pressure probe, manufactured especially for these measurements, is used to obtain time-averaged surveys of total pressure, static pressure, and the three mean velocity components. These data are then used to deduce distributions of streamwise vorticity. To obtain the surveys, the probe employed is mounted on an automated two-dimensional traverse, and inserted into the test section through a slot lined with foam to prevent air leakage. The centerline of this probe is traversed as close as about 5 mm from the test section top wall, and as close as approximately 5 mm from the test section bottom wall. The output ports of the probe are connected either to Validyne DP103-06 pressure transducers (to measure differential pressures up to 2.5 mm of water), or Celesco LCVR pressure transducers (to measure differential pressures up to 20.0 mm of water). Signals from the transducers are then processed by using Celesco CD10D Carrier-Demodulators. Voltages from the Carrier-Demodulators are acquired with a Hewlett-Packard 44422A data acquisition card installed in a Hewlett-Packard 3497A data acquisition control unit. This control unit, two Superior Electric type M092-FD310 Mitas stepping motors on the two-dimensional traverse, a Superior Electric Modulynx Mitas type PMS085-C2AR controller, and a Superior Electric Modulynx Mitas type PMS085-D050 motor drive are controlled by a Hewlett-Packard A4190A Series computer. Contour plots of measured quantities are generated by using a polynomial interpolating technique (with DeltaGraph software) between data points. In each survey plane, 1560 data points are spaced 2.54 mm apart. Data obtained at each one of these locations is time-averaged over a period of about 30 seconds.

2.4 Longitudinal turbulence intensity measurements and spectra of longitudinal velocity fluctuations

A single horizontal-type platinum-plated tungsten hot-wire sensor, with a diameter of 5.0 μm and a length of 2.54 mm, is employed to measure the time varying longitudinal component of velocity at the inlet of the test section and within the test section. The time-averaged longitudinal velocity, longitudinal turbulence intensity, and turbulence length scale are then determined from these measurements. When the probe traverses over a measurement plane, it is positioned and controlled by using the same two-dimensional traverse, controller, and drive as are employed with the five-hole pressure probe. When the hot-wire sensor is used to measure the turbulence intensity level, the sensor is located in the center of the channel cross-section (Z/H=0, Y/H=0.05), at X/H=6.27, which is just above downstream parts of dimples in the seventh streamwise row. The hot-wire probe is driven by a Disa 55M10 constant-temperature hot-wire anemometer bridge. The analog signal from this bridge is then processed using a Dantec 56N20 signal conditioner with a low-pass, anti-aliasing filter set to 1.0 kHz. The time-varying output voltage signal is then sampled at a 2.0 kHz rate by using a DATEL PCI441D I/O board installed in the Dell Precision 530 PC workstation. During each measurement, 60,000 voltage values are sampled over a 30 second period. Data are acquired by LABVIEW 6.1 software and then processed further with Matlab 6.1 software, including determination of the turbulence length scale. This is accomplished by integrating the autocorrelation functions which are deduced from the time-varying longitudinal velocity signals. The entire measurement system, including the hot-wire sensor, is calibrated along the centerline of the channel. A Kiel type pressure probe, wall static taps, and a copper-constantan thermocouple are used to measure and determine the total pressure, static pressure, static temperature, and streamwise velocity at the test section location where the calibration is conducted.

Power spectra density profiles of streamwise velocity fluctuations (u') are obtained from 4096 (2^{12}) point of Fast-Fourier-Transforms (FFT). Each power spectra density profile is determined from an ensemble average of 100 individual profiles obtained over overlapping time intervals which are spread over a total time period of 30 seconds.

2.5 Uncertainty estimates

Uncertainty estimates are based on 95 percent

confidence levels and are determined by using methods described by Moffat [19]. Uncertainty of temperatures measured with thermocouples is ±0.15 ° C. The experimental uncertainties of time-averaged magnitudes of local total pressure (relative to atmospheric pressure), local static pressure (relative to atmospheric pressure), local streamwise velocity, and local streamwise vorticity are ± 4.0, ± 4.0, ± 2.5, and ± 8.0 percent, respectively. The estimated uncertainties of the time-averaged magnitudes of the spanwise and normal velocity components are about ± 8.0 percent, and ± 10.0 percent, respectively. The estimated uncertainty of the time-averaged magnitude of the longitudinal Reynolds normal stress (or the mean-square of the fluctuating velocity component) is about ± 5.0 percent.

3. Experimental results and discussion

3.1 Instantaneous flow structure

Variations of instantaneous flow visualization images with Reynolds number are compared for dimple geometries according to three dimple depths in Fig. 2. These images are obtained at the same flow visualization location. Different ranges of Reynolds number are used for three dimple depths. This is because the images come out differently at different Reynolds number for different dimple depths: greater flow disturbances occur with deeper dimples; therefore, the Reynolds numbers used are lower, and similarly, higher Reynolds numbers are used for shallow dimples due to their lower disturbance. All three dimples produce the same classic structure of the flow. There is a primary vortex pair shedding at the central part of the dimple, and there are edge vortex pairs which advect downstream along the edge of the dimples. Notice that these are instantaneous images and all the dimpled images vary in time for all different Reynolds numbers. The biggest difference between images for different dimple depths is that, as the dimple depth becomes to be larger, the central primary vortex pairs seems to be a little bit more convoluted, more distorted, and the edge vortex seems to be bigger.

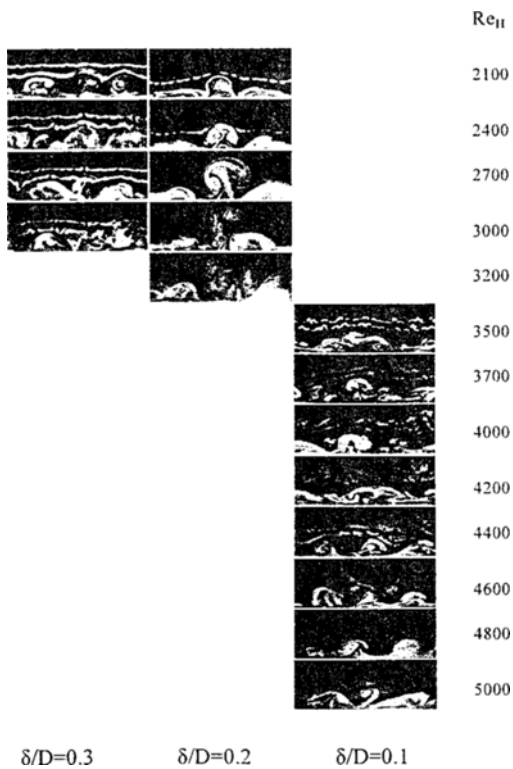

Fig. 2. Comparison of Instantaneous flow visualization images of dimples geometries with three different depths at different Reynolds numbers.

3.2 Time-averaged flow structure

Figs. 3(a) to 3f present surveys of time-averaged flow structure for three different dimple depths, δ/D=0.1 to 0.3 and Re_H= 20,000. These data are obtained by five hole pressure probe, which is positioned in a measurement plane just downstream of the seventh row of dimples, X/H=6.27, accordingly. These data are presented for a higher Reynolds number than those used to obtain the flow visualization data because overall experimental uncertainties are lower as Reynolds number increases. Surveys of streamwise velocity u_x [Fig. 3(a)], total pressure P_o [Fig. 3(b)] and static pressure P [Fig. 3(c)] show deficits near the central part of the dimple (Z/H=0). These results include the double deficits of normalized streamwise velocity and total pressure in the vicinity of Z/H=0 for δ/D=0.3, which are replaced by single deficits for δ/D=0.1 and δ/D=0.2. These double deficits presented near dimple edges for δ/D=0.3 are partially due to edge vortex pairs. Such edge vortex pairs increase in strength as the flows advect past multiple δ/D=0.3 dimples and the cumulative effects of multiple dimple rows are imposed. The spanwise and normal velocity component data [u_y and u_z in Figs. 3(d) and 3(e), respectively] are used to determine the distribution of

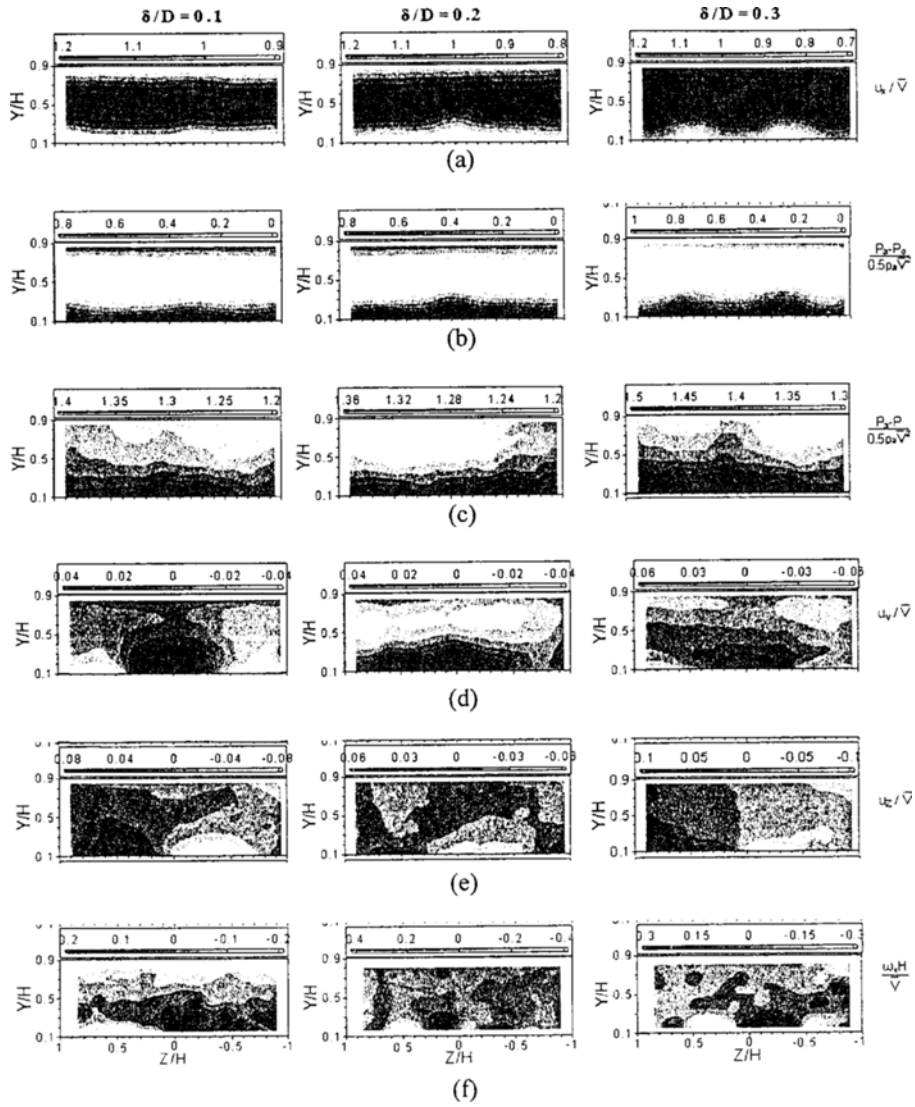

Fig. 3. Surveys of different time-averaged quantities measured in a spanwise-normal plane at X/H=6.27 just downstream of the downstream edge of dimples in the seventh row for δ/D =0.1 to 0.3, H/D=1, and Re_H=20,000. (a) Normalized streamwise velocity, (b) Normalized total pressure, (c) Normalized static pressure, (d) Normalized normal velocity, (e) Normalized spanwise velocity, (f) Normalized streamwise vorticity.

local streamwise vorticity ω_x shown in Fig. 3(f). Variations of normal and spanwise velocity components in Figs. 3(d) and 3(e) are mostly due to secondary flow motions from the different vortex pairs which develop in the channel. Notice the large positive magnitudes of normal velocity u_y located near Z/H=0, which evidence secondary flow motion away from the surface in the upwash region. These are positioned just above the central part of the dimpled surface at Y/H from 0 to 0.4. Spanwise velocity magnitudes u_z are then in the positive and negative directions on either side of this extended upwash region, depending mostly upon location within and relative to the upwash region and the primary vortex pair. Positive and negative regions of vorticity, associated with the primary vortex pair, like the ones seen earlier in flow visualization results, are readily apparent in Fig. 3(f). The variations of static pressure P [Fig. 3(c)], normal velocity u_y [Fig. 3(d)] and spanwise velocity u_z [Fig. 3(e)] are roughly the same for all three depths of dimples. There are larger deficits of total pressure P_o [Fig. 3(b)] and streamwise

velocity [Fig. 3(a)] with deeper dimples. This is apparently so near Y/H=0 where the dimples are located. There is some scattering in streamwise vorticity data, as shown in Fig. 3(f). However, all three dimple depths show the same distribution of vorticity even with the scattering of the data. Higher magnitude of streamwise vorticity is presented near Y/H=0.

Figs. 4(a) to 4(c) are obtained by using the hot-wire probe. These probes are positioned in a spanwise-normal measurement plane just downstream of the seventh row of dimples at X/H=6.27. Variations of normalized Reynolds normal stress $\overline{u'^2}/\overline{V^2}$ are presented in Fig. 4. Similar to distributions of the vorticity given in Fig. 3(f), the region of high magnitude of $\overline{u'^2}/\overline{V^2}$ is at the same location as the primary vortex pair. Also, Figs. 4(b) and 4(c) show one region of high spanwise-normalized Reynolds normal stress is very near the dimple surface at Z/H from -0.5 to +0.5 for the deep dimple (δ/D=0.3) and -0.1 to +0.1 for the medium dimple (δ/D=0.2) which are at the same locations as the primary vortex pair, the large extended upwash region evident in the $u_y/\overline{V}$ distribution, and the deficits of streamwise velocity and total pressure. But, for the shallow dimple (δ/D=0.1) in Fig. 4(a), Reynolds normal stress is slightly high at Z/H=0. The augmented normal stress levels occur thus due to increased production of turbulence kinetic energy, at locations where local shear magnitudes and strain rates are increased.

Fig. 5 shows the longitudinal component of Reynolds normal stress determined at a Reynolds number of 20,000. Data are given for dimples with three different dimple depths. Basically, at each Y/H the magnitude of this Reynolds normal stress increases as the depth of the dimple increases. This is especially so from Y/H=0.5 to Y/H=0, which is the region immediately above the dimples at the bottom part of the channel. Generally, this implies the turbulence transport increases as the depth of dimples increases, which is consistent with circulation and the vorticity magnitudes mentioned earlier in Fig. 3(f). The data for all three dimple depths show increases as Y/H decreases (approaches the surfaces with the dimples). Notice that at the top part of the channel, from Y/H=0.5 to 1, the distributions of Reynolds number of shallow, medium and deep dimples are roughly the same. This means the effects of the dimples are not very apparent at the top of the channel. It also implies the effects of the dimple occur within one half of the dimple print diameter which is located at less than Y/H=0.5.

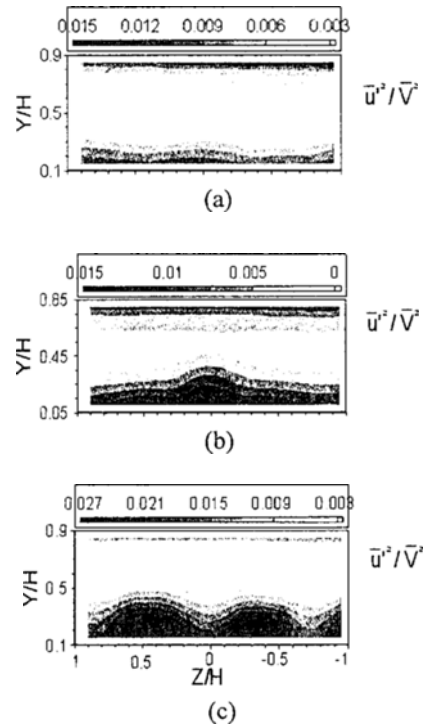

Fig. 4. Normalized Reynolds normal stress surveys of different time-averaged quantities measured in a spanwise-normal plane at X/H=6.27, just downstream of the downstream edge of dimples in the seventh row for Re_H=20,000 and H/D=1. (a) δ/D =0.1, (b) δ/D =0.2, (c) δ/D =0.3.

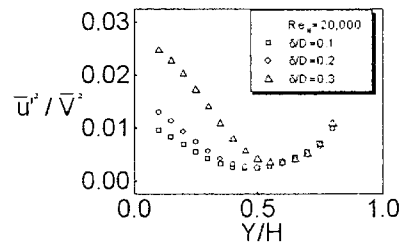

Fig. 5. The longitudinal component of Reynolds normal stress variations across the channel at Re_H=20,000 for three dimple depths.

3.3 Power Spectral Density (PSD) profiles and longitudinal frequencies

Three examples of ensemble-averaged power spectral density profiles of longitudinal velocity fluctuations are presented in Figs. 6(a) to 6(c) for three dimple depths at Re_H=20,000. The data is given for X/H=6.27, Y/H=0.05, Z/H=0 and 0.5, respectively,

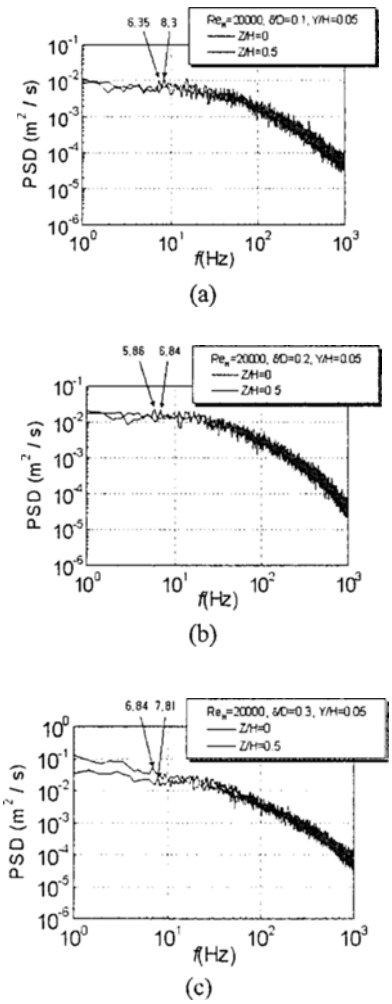

Fig. 6. Ensemble-averaged power spectral density profiles of longitudinal velocity fluctuations measured at X/H=6.27, Y/H=0.05, and Z/H=0, 0.5, respectively, just downstream of the downstream edge of dimples in the 7th row, for Re_H=20,000, H/D=1. (a) δ/D=0.1, (b) δ/D=0.2, and (c) δ/D=0.3.

Z/H=0 is downstream the centerline of the dimple; therefore, the data give information of the primary vortex pairs shedding from the central portion of the dimple. Z/H=0.5 is at a location of dimple spanwise edge, where it is mostly affected by the oscillation of the edge vortex pairs which are shed downstream the dimple in the same sequence of rows. As shown in Figs. 6(a) to 6(c), the energy level is decreasing as the frequency increases for all three dimple depths. That is a behavior of a typical turbulent flow. More importantly, PSD profiles exhibit several pronounced peaks which represent higher energy at particular

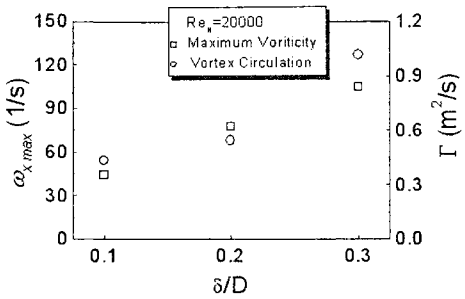

Fig. 7. Variation of maximum time-averaged streamwise vorticity and vortex circulation with Re_H =20000 for three different dimple depths. Data are given for the spanwise-normal plane at X/H=6.27, just downstream of the downstream edge of dimples in the seventh row for H/D=1.

frequencies. The first peak with predominant energy and substantial strength in each PSD profile is generally identified as the frequency. The frequency associated with the central vortex pair is 8.3 Hz for δ/D=0.1, 6.84 Hz for δ/D=0.2 and 7.81 Hz for δ/D=0.3, respectively. The frequency associated with the oscillation of the edge vortex pair is 6.35 Hz for δ/D=0.1, 5.86 Hz for δ/D=0.1, and 6.84 Hz for δ/D=0.3, respectively. The identification of these values is also consistent with flow visualization results like the ones shown in Fig. 2. Notice that a few rather pronounced peaks of higher frequencies are also discernible in each PSD profile.

Fig. 7 presents maximum streamwise vorticity values and circulation magnitudes with streamwise vorticity as they vary with Reynolds number and dimple depth. Maximum streamwise vorticity magnitudes $\omega_{x,max}$ are determined from time-averaged surveys such as the one shown in Fig. 3(f). Fig. 7 shows that maximum vorticity magnitudes increase as the Reynolds number increases for all three δ/D values, 0.1, 0.2, and 0.3. The highest maximum vorticity magnitudes at each Reynolds number are then associated with deep dimples (δ/D=0.3), which means that stronger time-averaged vortex structures are produced by deeper dimples. Stronger vortices generally give higher heat transfer augmentations because the associated secondary flows are greater. There is also greater shear and greater mixing which increase three-dimensional turbulent transport.

Circulation magnitudes associated with streamwise vorticity are also presented in Fig. 7, as they vary with Reynolds number for the three dimple depths. Circulation magnitudes Γ are determined from integrals of streamwise vorticity over spanwise-normal

rectangular areas covering the region where approximately one-half of the primary vortex pair is located. These data show the same trends as the maximum streamwise vorticity data in the previous figure, since they also increase with dimple depth at each Reynolds number, and increase with Reynolds number for each value of δ/D.

4. Summary and conclusions

Flow structure over dimple surfaces with three different depths in a rectangular channel is experimentally studied for Reynolds number based on channel height from 2,100 to 20,000. The ratios of dimple depth to dimple print diameter δ/D are 0.1, 0.2 and 0.3, respectively.

Flow Visualizations show substantial time varying behaviors of vortex pairs produced by dimples. For all three dimple depths, classic structure of the flow is observed: there is a primary vortex pair shedding at the central part of the dimple, and there are edge vortex pairs which advect downstream the edge of the dimples. Instantaneous flow visualization images show that the central primary vortex pairs are more convoluted, distorted, and the edge vortex seems to be bigger as the dimple depth becomes to be larger.

Surveys of time-averaged distributions of different components of local velocity, local total pressure, local static pressure, and local streamwise vorticity provide consistent evidence of the existence and location of the primary vortex pair. There are larger deficits of total pressure and streamwise velocity with deeper dimples. As the dimple depth increases, higher magnitudes of streamwise vorticity, vortex circulation and Reynolds normal stress are obtained, which implies stronger vortices and increasing turbulence transport associated with the increase of the depth of dimples.

Ensemble-averaged power spectral density profiles of longitudinal velocity fluctuations present additional information on the unsteadiness associated with the vortices shed from the dimples. Identified from these PSD profiles, primary vortex shedding frequencies ranges from 7 to 9 Hz, and edge vortex pair oscillation frequencies range from 5 to 7 Hz. Due to the unsteadiness of vortex shedding, no consistent trend with the dimple depth is found for the range of Reynolds number tested.

Nomenclature

a : Streamwise extent of test surface
b : Spanwise extent of test surface
D : Dimple print diameter
f : Frequency
H : Channel height
p : Streamwise spacing of adjacent dimple rows
P : Local static pressure
P_O : Local total pressure
P_a : Ambient atmospheric pressure at test section inlet
PSD : Power Spectra Distribution
Re_H : Reynolds number based on channel height, $H\overline{V}/\nu$
s : Streamwise spacing of every other dimple row
t : Time
t* : Non-dimensional time, $t\overline{V}/H$
T : Temperature
u : Local streamwise instantaneous velocity
u_x : Local time-averaged streamwise component of velocity
u_y : Local time-averaged normal component of velocity
u_z : Local time-averaged spanwise component of velocity
$\overline{V}$: Streamwise bulk velocity averaged over the channel cross-section
X : Streamwise coordinate measured from test section inlet
Y : Normal coordinate measured from test surface dimple horizon
Z : Spanwise coordinate measured from test section center-line
ν : Kinematic viscosity
δ : Dimple depth
ω_x : Local time-averaged streamwise vorticity

References

[1] V. N. Afanasyev, Y. P. Chudnovsky, A. I. Leontiev and P. S. Roganov, Turbulent flow friction and heat transfer characteristics for spherical cavities on a flat plate, *Experimental Thermal and Fluid Science.* 7 (1993) 1-8.

[2] M. Y. Belen'kiy, M. A. Gotovskiy, B. M. Lekakh, B. S. Fokin and K. S. Dolgushin, Heat transfer augmentation using surfaces formed by a system of spherical cavities, *Heat Transfer Research.* 25 (2) (1994) 196-203.

[3] V. S. Kesarev and A. P. Kozlov, Convective heat

transfer in turbulized flow past a hemispherical cavity, *Heat Transfer Research.* 25 (2) (1994) 156-160.

[4] V. I. Terekhov, S. V. Kalinina and Y. M. Mshvidobadze, Flow structure and heat transfer on a surface with a unit hole depression, *Russian Journal of Engineering Thermophysics.* 5 (1995) 11-33.

[5] A. V. Schukin, A. P. Koslov and R. S. Agachev, Study and application of hemispherical cavities for surface heat transfer augmentation, ASME Paper No. 95-GT-59, ASME 40th International Gas Turbine and Aeroengine Congress and Exposition, Houston, Texas (1995).

[6] Y. F. Gortyshov, I. A. Popov, R. D. Amirkhanov and K. E. Gulitsky, Studies of hydrodynamics and heat exchange in channels with various types of intensifiers, Proceedings of 11th International Heat Transfer Congress, 6 (1998) 83-88.

[7] Y-L. Lin, T. I-P. Shih and M. K. Chyu, Computations of flow and heat transfer in a channel with rows of hemispherical cavities, ASME Paper No. 99-GT-263, ASME 44th International Gas Turbine and Aeroengine Congress and Exposition, Indianapolis, Indiana, (1999).

[8] H-K. Moon, T. O'Connell and B. Glezer, Channel height effect on heat transfer and friction in a dimpled passage, ASME Paper No. 99-GT-163, ASME 44th International Gas Turbine and Aeroengine Congress and Exposition, Indianapolis, Indiana, (1999).

[9] G. I. Mahmood, M. L. Hill, D. L. Nelson, P. M. Ligrani, H-K. Moon and B. Glezer, Local heat transfer and flow structure on and above a dimpled surface in a channel, *ASME Transactions-Journal of Turbomachinery.* 123 (1) (2001) 115-123.

[10] V. I. Terekhov and S. V. Kalinina, Flow and heat transfer in a single spherical cavity: state of the problem and unanswered questions (Review), *Thermophysics and Aeromechanics.* 9 (4) (2002) 475-496.

[11] G. I. Mahmood, M. Z. Sabbagh and P. M. Ligrani, Heat transfer in a channel with dimples and protrusions on opposite walls, *AIAA Journal of Thermophysics and Heat Transfer.* 15 (3) (2001) 275-283.

[12] P. M. Ligrani, G. I. Mahmood, J. L. Harrison, C. M. Clayton and D. L. Nelson, Flow structure and local Nusselt number variations in a channel with dimples and protrusions on opposite walls, *International Journal of Heat and Mass Transfer.* 44 (23) (2001) 4413-4425.

[13] S. A. Isaev, A. I. Leontiev, N. A. Kudryavtsev and I. A. Pushnyi, The effect of rearrangement of the vortex structure on heat Transfer under conditions of increasing depth of a spherical dimple in the wall of a narrow channel, *Teplofizika Vysokikh Temperature.* 41 (2) (2003) 268-272.

[14] S. Y. Won and P. M. Ligrani, Numerical predictions of flow structure and local Nusselt number ratios along and above dimpled surfaces with different dimple depths in a channel, *Numerical Heat Transfer Part A.* 46 (2004) 549-570.

[15] N. K. Burgess, M. M. Oliveira and P. M. Ligrani, Nusselt number behavior on deep dimpled surfaces within a channel, *ASME Transactions-Journal of Heat Transfer.* 125 (1) (2003) 11-18.

[16] G. I. Mahmood and P. M. Ligrani, Heat transfer in a dimpled channel: combined influences of aspect ratio, temperature ratio, Reynolds number, and flow structure, *International Journal of Heat and Mass Transfer.* 45 (10) (2002) 2011-2020.

[17] P. M. Ligrani, J. L. Harrison, G. I. Mahmood and M. L. Hill, Flow structure due to dimple depressions on a channel surface, *Physics of Fluids.* 13 (11) (2001) 3442-3451.

[18] P. M. Ligrani, Flow visualization and flow tracking as applied to turbine components in gas turbine engines, *Meas. Sci. Technol.* 11 (2002) 992.

[19] R. J. Moffat, Describing the uncertainties in experimental results, *Experimental Thermal and Fluid Science.* 1 (1) (1988) 3-17.